Supporting Information

Prolate Spheroidal Polystyrene Nanoparticles: Matrix Assisted Synthesis, Interface Properties, and Scattering Analysis

Dominik Benke, [†a] Tanja Feller, [†a] Marcel Krüsmann, [†b] Anna M. Neuhöfer, [a] Friederike Ganster, [a] Matthias Karg, [b] Markus Retsch [a,c]

a. *Department of Chemistry, Chair of Physical Chemistry 1, University Bayreuth, E-mail: retsch@uni-bayreuth.de , Homepage: http://www.retsch.uni-bayreuth.de.*
b. *Chair of Colloids and Nano Optics, Heinrich-Heine-University Düsseldorf, D-40225 Düsseldorf, Germany.*
c. *Bavarian Polymer Institute, Bayreuth Center for Colloids and Interfaces, Bavarian Center for Battery Technology (BayBatt), Universitätsstraße 30, 95447 Bayreuth, Germany*

† Dominik Benke, Tanja Feller, and Marcel Krüsmann contributed equally to this publication.
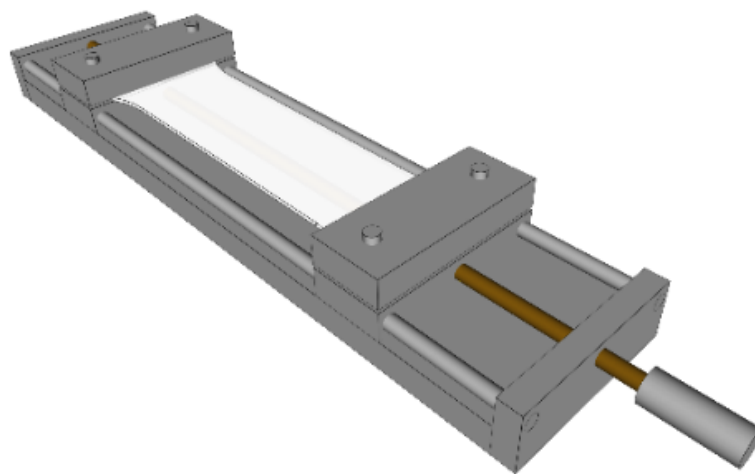
Home build stretching device

Figure S1. CAD reconstruction of the home-build stretching device. CAD construction file can be sent on request.

On each side, a clamp holds the foil elevated above the frame. The clamps are two steel blocks screwed together. The sides facing the foil are sandblasted to avoid slipping of the foil, which is especially crucial when using thick or multiple stacked foils. Foils were either clamped completely or just to the middle of the clamps. The clamps can be moved apart by turning the handle of a brass spindle connecting the clamps. Multiple lengths of the stretching device were built to handle different lengths of stretched foils.

Foils after stretching

The rectangular foil pieces of e.g. 8 × 4 cm, were marked with 5 mm squares. After stretching, the middle part in-between the 1.5 cm lines (1st line next to the black one) from the clamped sides is stretched equally and therefore used to recover the particles. A pencil was used for marking the inner part, as it can be erased after stretching, while a normally used permanent marker cannot be erased after heating and therefore colours the particles.

The 1.5 cm distance to the 1st inner pencil line is sufficient to account for the necking behaviour of the film at 150 °C (bone shape, Figure S2 A and B). In between these parts, the width does not strongly decrease any further. Ho et al.[1] inferred that necking could be lower at higher temperatures. This was confirmed when an intermediate metal block was implemented on a long stretching device (Figure S2C). The part above this block stayed wider than the rest, leading to uneven stretching, especially when aiming for a higher aspect ratio. Such a design of the stretching device should, therefore, be avoided.
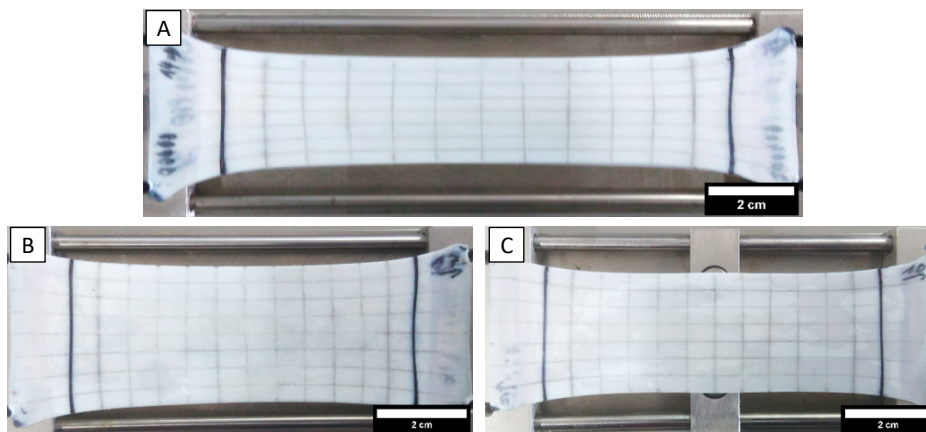

Figure S2. Examples of stretched Foils. For recovering the particles, just the inner part (from 1st to last pencil line) is used. **A** Foil after 108% stretching = aspect ratio 4, **B** foil after 36% stretching = aspect ratio 2, and **C** foil stretched to 36% but with a metal block below the middle of the foil leading to a slightly wider middle part; scale bars 2 cm

Analysis of DLS data from spherical particles

The spherical particles (PS spheres, embedded and embedded & heated) were studied by angle-dependent DLS. Figure S3A shows exemplary intensity-time autocorrelation functions measured at a scattering angle θ = 20 °. Monomodal decays are observed for all three samples and the correlation functions nearly overlap. The inflection points, that roughly correspond to the relaxation times, are very similar between different samples. Slight mismatches between the correlation functions are mostly related to the differences in intercept, β. Figures S3B-D shows the diffusion analysis in terms of relaxation rates Γ determined from cumulant analysis[2] as a function of the squared magnitude of the scattering vector. The solid lines are linear fits to the data with fixed intercept of zero. As expected for isotropic, homogeneous objects purely translational motion is probed in the respective range of q. Consequently, the slopes of the linear fits correspond to the translational diffusion coefficients D_T:

$$D_{\mathrm{T}} = \frac{\Gamma}{q^2} \qquad \qquad \text{(eq. S1)}$$

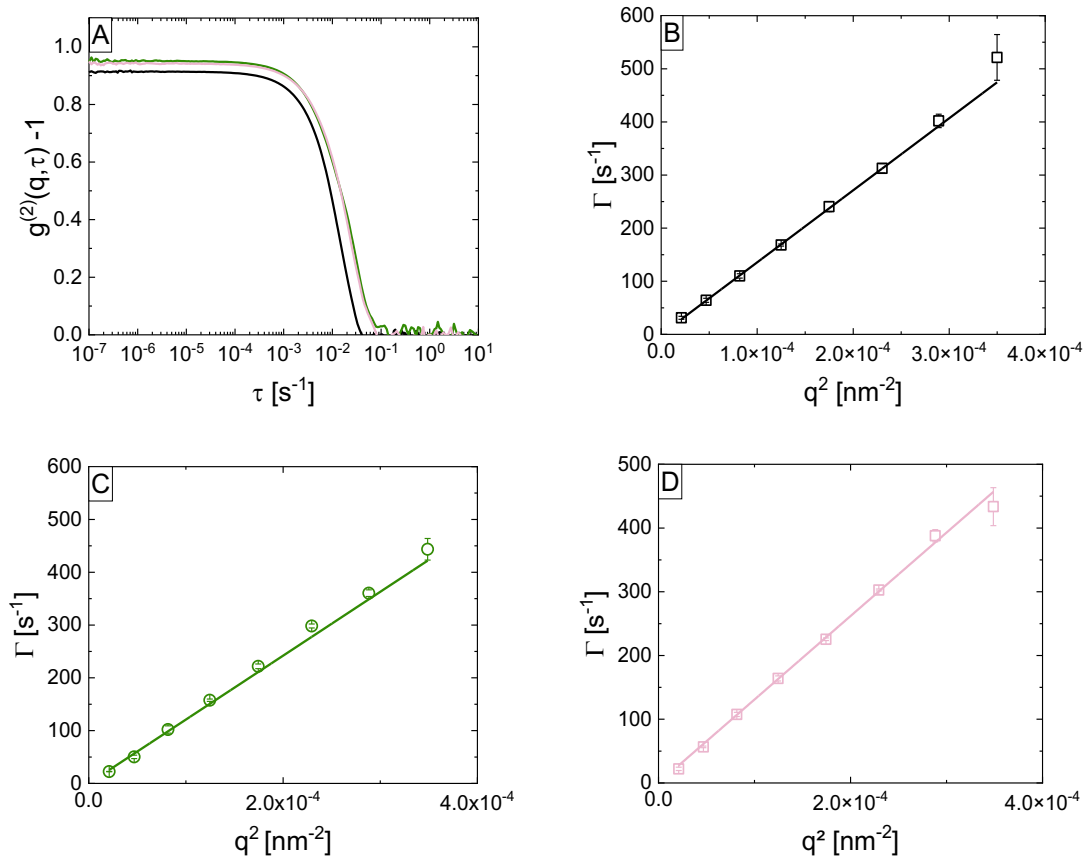**Figure S3. A** Intensity-time autocorrelation functions from DLS measurements at θ = 20° from PS spheres (black), embedded (green) and embedded & heated (light pink). Relaxation rates Γ from cumulant analysis as a function of the squared magnitude of the scattering vector for PS spheres (**B**), embedded particles (**C**) and embedded & heated particles (**D**). The results shown correspond to scattering angles θ of 20 – 90 °. The colour code for the different samples is the same as in the main manuscript. The solid lines represent linear fits to the data where the intercept was fixed to zero.

Hydrodynamic radii R_h were calculated from values of D_T using the Stokes-Einstein equation:

$$D_T = \frac{k_B T}{6\pi\eta R_h}$$ (eq. S2)

Here, k_B is the Boltzmann constant, T the absolute temperature and η refers to the dynamic viscosity of the surrounding medium, i.e. water in our case with a value of 0.89 mPas at 298.15 K. The respective results (R_h) are listed in Table 2 in the main manuscript.

Analysis of DLS and DDLS data from non-spherical particles (Ellipsoids)

The autocorrelation functions from standard DLS (VV polarization) and from DDLS (VH polarization) can be described as follows:

$$g_{VV}^{(1)}(q,\tau) = S_0 \, exp(-D_T q^2 \tau) + S_2 \, exp(-(D_T q^2 + 6D_R)\tau) \quad \text{(eq. S3)}$$

$$g_{VH}^{(2)}(q,\tau) - 1 = \beta \exp(-2(q^2 D_T + 6D_R)\tau) \quad \text{(eq. S4)}$$

Here, τ is the delay time, D_T and D_R are the translational and rotational diffusion coefficients and S_1 and S_2 are scaling coefficients. While for slender bodies where $ql < 5$ correlation functions from DLS (VV) are expected to be single exponentials with only contributions from translational motion ($S_2 = 0$), for $5 < ql < 10$ higher order modes become relevant and correlation functions are expected to be bimodal. The q-range in our light scattering experiments corresponding to scattering angles of 20 – 140 ° is 0.0046 – 0.0248 nm^{-1}. Our prolate spheroids with l ranging from 556 to 901 nm (value from SEM) strictly only met the condition $ql < 5$ at small scattering angles.

Figure S4 and S5 show representative autocorrelation functions from DLS (S5) and DDLS measurements (S4) performed at θ = 20 °. The solid lines correspond to the respective fits based on eq. S3 and eq. S4, respectively.
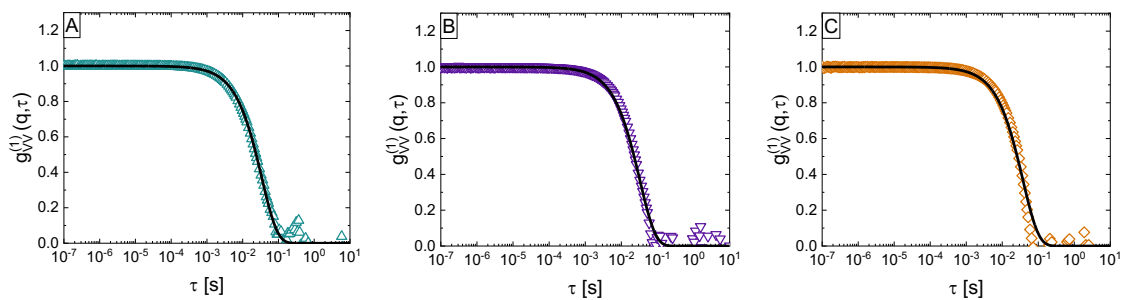

Figure S4. Field-time autocorrelation functions from DLS measurements (VV) at 20 ° for the 2:1 Ellipsoids (**A**), the 3:1 Ellipsoids (**B**) and the 4:1 Ellipsoids (**C**). Solid lines are respective fits to the data.
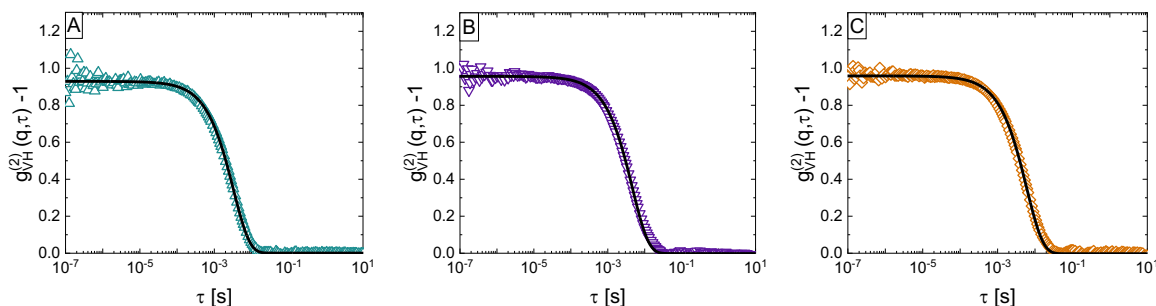
Figure S5. Intensity-time autocorrelation functions from DDLS measurements (VH) at 20 ° for the 2:1 Ellipsoids (**A**), the 3:1 Ellipsoids (**B**) and the 4:1 Ellipsoids (**C**). Solid lines are respective fits to the data.

The fits match the experimental data, and all correlation functions appear monomodal. For the DLS data (Figure S5) recorded at θ = 20 ° $ql < 5$ is fulfilled, and therefore the correlation functions should be dominated by the translational diffusion. At larger scattering angles, it is expected that the higher-order modes become relevant ($S_2 \neq 0$). Therefore, we first analyze the DLS data as suggested by Nixon-Luke and Bryant[3]. Figure S6 shows field-time autocorrelation functions from DLS measurements (VV) of the three samples (Ellipsoids) over the whole angular range (20 – 140 °) in 10 ° steps and plotted over $q^2\tau$. At large scattering angles (towards the red), the functions become multimodal and shift towards larger decay times.
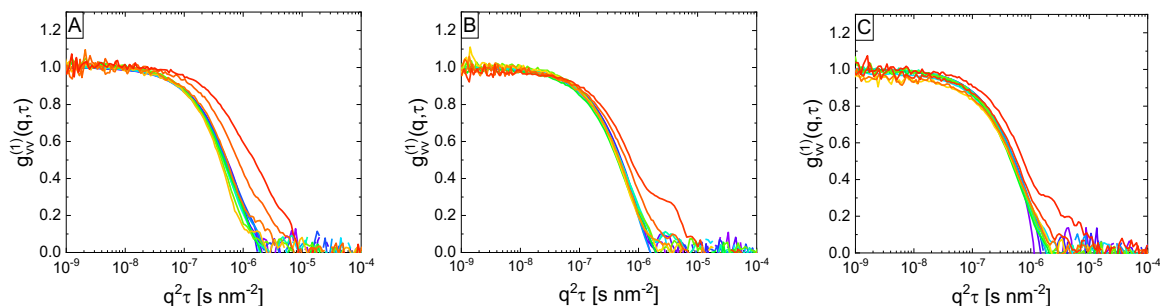

Figure S6. Field-time autocorrelation functions $g_{VV}^{(1)}$ plotted against q²τ for scattering angles from 20 - 140° in 10 ° steps for 2:1 Ellipsoids (**A**), for 3:1 Ellipsoids (**B**) and 4:1 Ellipsoids (**C**). The scattering angle increases from violet to red in each diagram.

Figure S7 shows the same data as Figure S6 but only for a selected range of angles (20 – 70 °) where the correlation functions collapse onto a mastercurve at larger decay times where the component from translational diffusion is expected to be dominant. For this range of angles, the determination of D_T is expected to be reliable.[3] It is worth noting that the correlation functions also overlap nicely at small decay times. This is different compared to data from DLS measurements on smaller anisotropic objects e.g. gold nanorods where the rotational diffusion coefficient D_R is significantly larger.[4]

The correlation functions shown in Figure S7 were then used to extract values of D_T by fitting the data with the above-mentioned equation S3 for $g_{VV}^{(1)}(q,\tau)$.
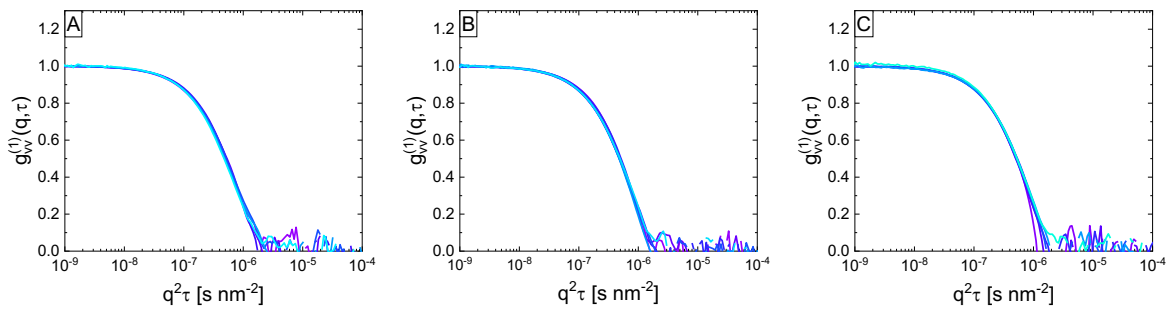

Figure S7. Selected $g_{VV}^{(1)}$ plotted against $q^2\tau$ only showing the angles from 20 – 70° where the long-time decay fully collapses onto a master curve for 2:1 Ellipsoids (**A**), for 3:1 Ellipsoids (**B**) and 4:1 Ellipsoids (**C**). The scattering angle increases from violet to light blue.

The obtained values of D_T were then used as fixed input parameters to fit the correlation functions from DDLS using the equation S4 for $g_{VH}^{(2)}(q,\tau)$ to determine the rotational diffusion coefficients D_R.

Figure S8 summarizes the results of the obtained D_T and D_R in dependence of q. Please note that the range of q used is the same corresponding to scattering angles of 20 – 70 ° while the DDLS data were measured in angular increments of 5 °. The solid lines correspond to the q-averaged mean values.
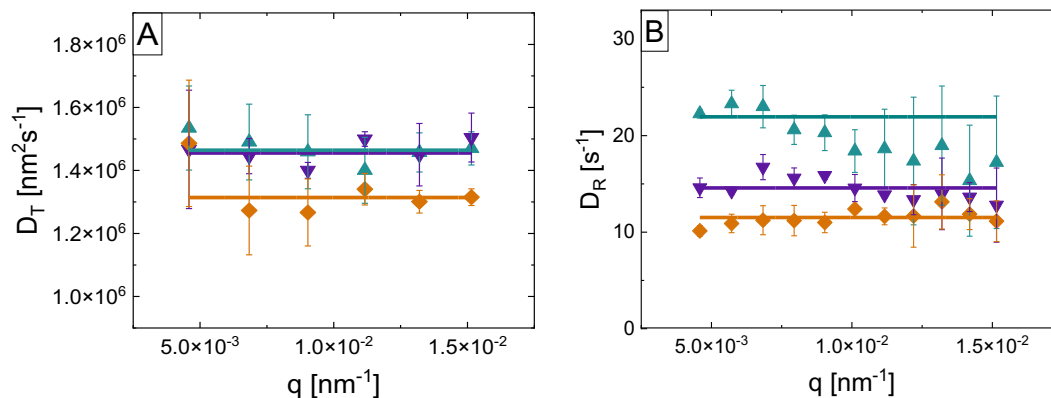

Figure S8. Translational (**A**) and rotational (**B**) diffusion coefficients from combined analysis of DLS and DDLS data in dependence of q for the different samples. Solid lines correspond to linear fits with slope zero, i.e. the average values.

In addition to the analysis procedure of DLS/DDLS data from Nixon-Luke and Bryant, we used the more "standard" analysis where relaxation rates are analysed in dependence of q^2. This seems well justified at least for the range of angles plotted in Figure S7 where all correlation functions appear monomodal. Similar to the procedure used above, DLS data are used to extract D_T, which can then be used to extract D_R from DDLS data:

$$\Gamma_{\text{DLS}} = q^2 D_{\text{T}} \qquad\qquad \text{(eq. S5)}$$

$$\Gamma_{\text{DDLS}} = q^2 D_{\text{T}} + 6 D_{\text{R}} \qquad\qquad \text{(eq. S6)}$$

The respective relaxation rates Γ were determined by cumulant analysis of the measured DLS and DDLS data. Figure S9 shows the respective results as a function of q^2.
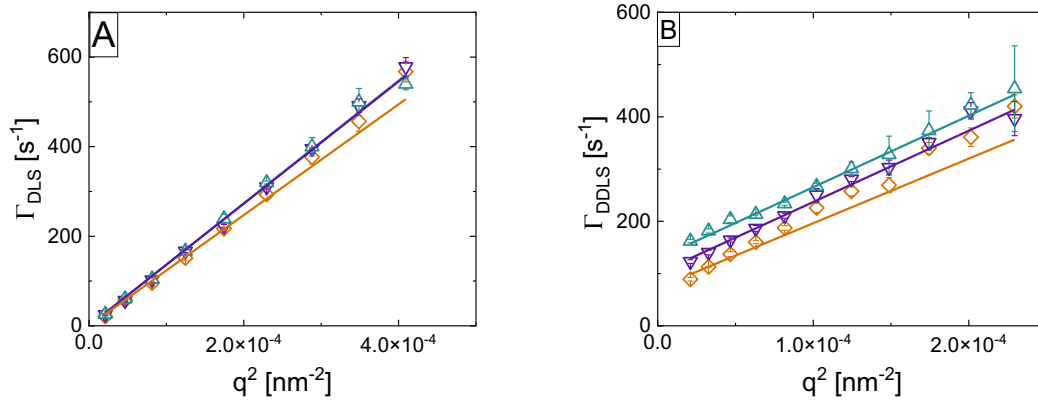

Figure S9. Relaxation rates from cumulant analysis of DLS (**A**) and DDLS data (**B**) plotted as a function of the squared magnitude of the scattering vector. Shown are data for scattering angles of 20 – 90 ° (**A**) and 20 – 70 ° (**B**). Solid lines represent linear fits to the data. In **A** the intercept was fixed to zero. In **B** the linear fits were performed with fixed slopes (D_{T}) as obtained from the linear fitting shown in **A**.

Figure S9A shows the expected linear scaling for translational diffusion over the whole range of plotted angles (20 – 90°) for the 2:1 Ellipsoids (green) and the 3:1 Ellipsoids (purple). At larger scattering angles than 90 ° the relaxation times start to scatter significantly with pronounced deviations from the linear behavior and, therefore, these data were not included in the analysis. For the 4:1 Ellipsoids (orange), the linear scaling is best at low angles and deviations towards larger angles (60 – 90 °) are observed. For the smaller particles the linear scaling is well fulfilled even to scattering angles of 90 °, i.e. slightly larger than the range in Figure S7. The same trend is observed in Figure S9B where the slopes of the linear fits were fixed using the values of D_{T} determined from the analysis in Figure S9A. The fits nicely match the data for the two shorter Ellipsoids while significant deviations are found for the 4:1 Ellipsoids, in particular at larger values of q^2, i.e. larger scattering angles. Here the same range of angles (20 – 70 °) was used as in our previous DDLS analysis. Table S1 summarizes the results from this analysis in direct comparison to the results from the analysis according to Nixon-Luke and Bryant and to theoretical values obtained from a model of prolate spheroids (Perrin) using the particle dimensions obtained from SEM analysis (see table 1 in the main manuscript).

Table S1. Diffusion coefficients from different analysis of DLS and DDLS data in comparison to calculated values using the theory of prolate spheroids (Perrin).

Sample	Cumulant (standard)		Nixon-Luke		Theory	
	$D_{T,DLS}$ [µm²/s]	D_R [s^{-1}]	D_T [µm²/s]	D_R [s^{-1}]	D_T [µm/s]	D_R [s^{-1}]
2:1	1.37 ± 0.02	21.4 ± 0.24	1.46 ± 0.01	22.0 ± 0.4	1.40	25
3:1	1.36 ± 0.01	16.8 ± 0.37	1.46 ± 0.02	14.6 ± 0.3	1.30	16
4:1	1.14 ± 0.02	12.1 ± 0.16	1.31 ± 0.01	11.5 ± 0.3	1.19	10

The results from the two different analysis procedures of the DLS and DDLS data differ stronger than their (small) standard variations in all cases. Stronger deviations are found for values of D_T. Nevertheless, the values are in quite good agreement. Overall, the values from "standard" analysis match better to the theoretical prediction. Therefore, those values are discussed in the main text.

We can also treat the DDLS data independently from the DLS data and fit the data shown in Figure S9 without values of D_T as fixed input parameters for the slope.[5]

Figure S10 shows the respective data with linear fits using slope and intercept as variable fitting parameters.
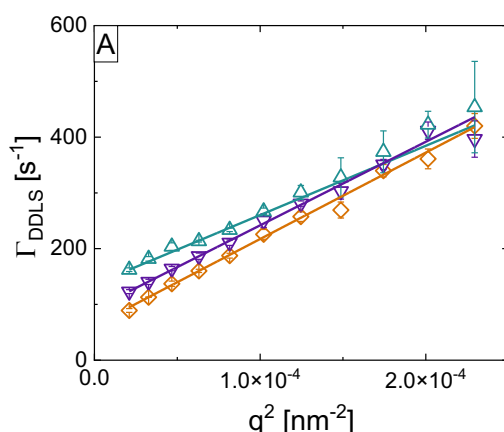

Figure S10. Relaxation rates from cumulant analysis DDLS data plotted as a function of the squared magnitude of the scattering vector. Shown are data for scattering angles of 20 – 90 °. Solid lines represent linear fits to the data

Table S2. Diffusion coefficients from independent analysis of DLS and DDLS based on relaxation rates obtained from cumulant analysis.

Sample	Cumulant (standard)		
	$D_{T,DLS}$ [µm²/s]	$D_{T,DDLS}$ [µm²/s]	D_R [s^{-1}]
2:1	1.37 ± 0.02	1.24 ± 0.05	22.7 ± 0.6
3:1	1.36 ± 0.01	1.50 ± 0.03	15.3 ± 0.4
4:1	1.14 ± 0.02	1.55 ± 0.03	10.4 ± 0.2

While the values of D_R from this independent analysis are close to the ones for the two other analysis as reported in Table S1, values of D_T deviate significantly. Importantly, values from the DDLS data, $D_{T,DDLS}$, increase with increasing aspect ratio which is the opposite of what is expected.

Evaluating different samples

Inter-sample reproducibility is given, as the average aspect ratio does not change much with the different stretched foil samples. It was, therefore, possible to merge the samples.
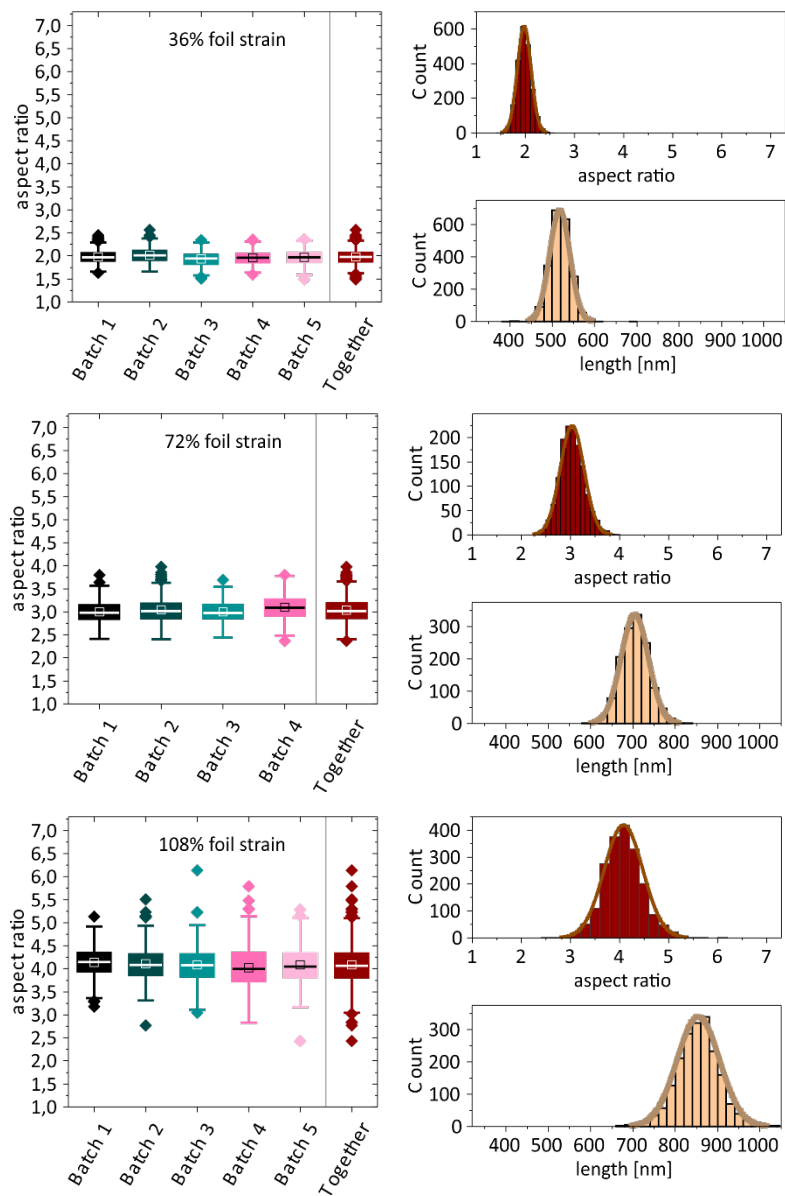

Figure S11. Boxplots of the different samples and their aspect ratio and size distribution of the merged batches ("Together").

Formulas used for calculating the corresponding sphere

For an ellipsoid, the formula of basic math has three different axis-radii (x, y, z). If we alter just one dimension (x; stretching direction), two of those radii will remain the same (y = z).

$$V = \frac{4}{3}\pi(x \cdot y^2) \qquad \text{(eq. S7)}$$

To calculate the volume of the corresponding sphere, we have to use the basic math formula for a sphere:

$$V = \frac{4}{3}\pi r^3 \qquad \text{(eq. S8)}$$

From the SEM images we can identify x as half of the length l and y as half of the width w. To calculate the diameter d of the corresponding sphere, the above-mentioned formula can be combined with the length l and width w of the particle to

$$d = 2 \cdot (x \cdot y^2)^{\frac{1}{3}} = 2 \cdot \left(\frac{l}{2} \cdot \left(\frac{w}{2} \right)^2 \right)^{\frac{1}{3}} \qquad \text{(eq. S9)}$$

The error is then calculated by error propagation

$$\Delta d = \sqrt{ \left(\left(\frac{1}{3} \cdot \left(\frac{w}{l} \right)^{\frac{2}{3}} \right) \cdot \Delta l \right)^2 + \left(\left(\frac{2}{3} \cdot \left(\frac{l}{w} \right)^{\frac{1}{3}} \right) \cdot \Delta w \right)^2 } \qquad \text{(eq. S10)}$$

Flow Field Fractionation (FFF)
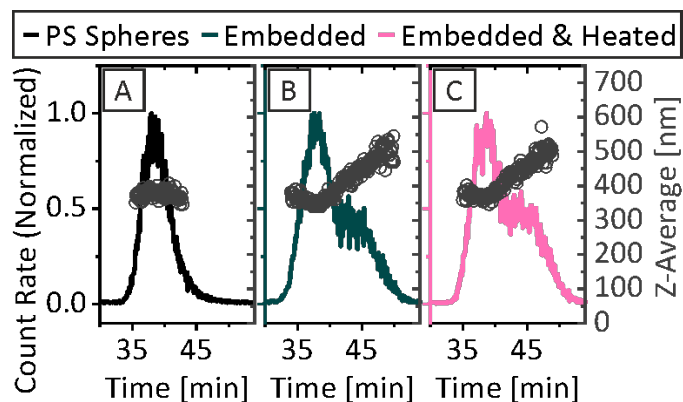
Additional graphs of the FFF measurements.

Figure S12. The on-line UV-VIS detector of **A** the pristine spherical particles before embedding in comparison to a **B** embedded and a **C** embedded & heated sample.
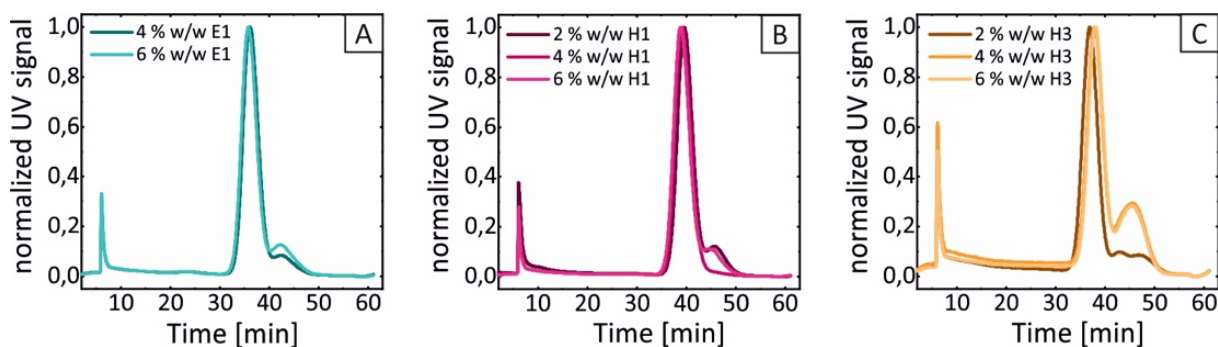

Figure S13. UV signal for the **A** just embedded, **B** 1 hot-wash treated and **C** 3 hot-wash treated spherical particle samples. One can identify that with increasing particle concentration in the foil (from 2 to 6 wt%) most samples show more agglomerates.

Bibliography

1. C. C. Ho, M. J. Hill and J. A. Odell, *Polymer*, 1993, **34**, 2019-2023.
2. B. J. Frisken, *Appl. Opt.*, 2001, **40**, 4087-4091.
3. R. Nixon-Luke and G. Bryant, *Particle & Particle Systems Characterization*, 2019, **36**, 1800388.
4. D. Feller, M. Otten, M. Hildebrandt, M. Krusmann, G. Bryant and M. Karg, *Soft Matter*, 2021, **17**, 4019-4026.
5. I. Martchenko, H. Dietsch, C. Moitzi and P. Schurtenberger, *J. Phys. Chem. B*, 2011, **115**, 14838-14845.